



GSV-SRTS: A Heterogeneous Landscape Soil-Canopy Reflectance Model Over Sloping Terrain with an Extended GSV and Stochastic Radiative Transfer Theory

Siqi Li¹, Guyue Hu^{1,2,*}, Shaoda Li¹, Ronghao Yang¹, Junxiang Tan¹, Chenghao Liu¹, Jinhu Bian^{2,3}

5 ¹College of Earth and Planetary Sciences, Chengdu University of Technology, Chengdu 610059, China

²Wanglang Mountain Remote Sensing Observation and Research Station of Sichuan Province, Mianyang 621000, China

³Institute of Mountain Hazards and Environment, Chinese Academy of Sciences, Chengdu 610213, China

Correspondence to: Guyue Hu (hugy@cdut.edu.cn)

Abstract. Accurately modelling radiation interactions within canopy layers and soil backgrounds is crucial for biophysical variables retrieval across regional or global scales. However, terrain relief can introduce significant uncertainties into forward radiative transfer modeling. Despite the development of numerous canopy reflectance models for sloping terrain, the heterogeneous characteristics of soil-canopy objects have often been overlooked, leading to distortions in the bidirectional reflectance distribution in small-scale landscapes. In this study, we present a canopy reflectance model suitable for heterogeneous structures on sloping terrain. By extending the stochastic radiative transfer theory from flat terrain to sloping terrain and integrating the soil General Spectral Vector, the GSV-SRTS model was introduced. This enables accurate prediction of soil-canopy radiative transfer within subpixel 3-D heterogeneous mountain landscapes. The proposed GSV-SRTS model was evaluated against the Discrete Anisotropic Radiative Transfer (DART) model, compared with typical mountain canopy reflectance models, and validated against remote sensing observations at varying spatial resolutions. The results showed that the GSV-SRTS model achieves good accuracy in the comparisons with DART ($R^2 = 0.9136$ (0.9052) and root-mean-square errors (RMSE) = 0.0246 (0.0216) in the red (NIR (Near-Infrared)) band) and performs well in real mountainous areas, particularly with high spatial resolution remote sensing observations ($R^2 = 0.9078$ (0.9143) and RMSE = 0.0201 (0.0212)). Furthermore, the GSV-SRTS model effectively captures the impacts of canopy structure and terrain factors on bidirectional reflectance. This underscores the GSV-SRTS model as a reliable physical tool for simulating radiation regimes over sloping terrain, with the potential to enhance the accuracy of biophysical variable retrieval from remote sensing observations.

25 1 Introduction

Canopy reflectance (CR) models simulate radiative transfer within vegetation-soil systems to link biophysical parameters with remote sensing data (Widlowski et al., 2013). Accurate simulation of these processes is fundamental for interpreting remote sensing observations and retrieving biophysical variables across scales (Verrelst et al., 2015). However, to manage the inherent



heterogeneity of reality, CR models necessarily employ abstractions and simplifications (Yin et al., 2017), which consequently
30 limits their ability to characterize fine-scale landscape details.

In addition, topography presents challenges in CR modeling, as terrain relief modifies illumination and viewing geometry, leading to variations in reflected radiance through surface anisotropic reflectance (S. Sandmeier, 1997), and significantly affecting the gap probability of canopy layers, which alters radiation contributions from both the canopy and soil background in solar and viewing directions (Wen et al., 2018). Therefore, the heterogeneous landscapes and sloping terrain are the primary
35 sources of uncertainty in CR modeling (Yin et al., 2017).

In recent decades, a variety of models for canopy reflectance on sloping terrain have been developed. Schaaf et al. (1994) introduced the geometric-optical (GO) and mutual shadowing models to sloping terrain (GOMST) by applying the coordinate rotation (Schaaf et al., 1994). Combal et al. (2000) expanded the Ross model (Ross, 2012) to account for sloping terrain while maintaining geotropic vegetation growth (Bruno Combal, 2000). Verhoef and Bach (2007, 2012) developed a framework that
40 integrated radiative transfer (RT) processes within within a soil-leaf-canopy (SLC) medium and later extended this model to sloping terrain (SLCT) (Verhoef and Bach, 2007) (Verhoef and Bach, 2012). However, these CR models overlooked the impact of the heterogeneity of canopy structure and soil properties and assumes that they are uniformly distributed in pixels.

The characterization of canopy heterogeneity structure is a crucial aspect in remote sensing studies. The geometric-optical model over sloping terrain (GOST) has been utilized to represent the realistic 3-D structure of canopy (Fan et al., 2014).
45 However, the computational complexity of GOST has limited its performance in parameter retrieval. The canopy reflectance model suitable for both continuous and discontinuous canopies over sloping terrain (BOST) was developed (Hu and Li, 2022). However, the internal canopy structure was based on the assumption of turbid media which inherited from the SLC model. To overcome these limitations, the Stochastic Radiative Transfer (SRT) theory was drawn into canopy RT modeling, which simulates the random scattering and absorption of photons as they interact with various canopy elements, allowing for a more
50 realistic representation of the three-dimensional (3D) structure of vegetation (Shabanov et al., 2000). This makes SRT a suitable approach for complex and heterogeneous scenarios (Shabanov et al., 2007). Zeng et al. developed a RT model specifically designed for patchy landscapes based on SRT theory (Zeng et al., 2020), which considered landscape heterogeneity by integrating stochastic processes to simulate radiation interactions within fragmented vegetation canopies, addressing variability in canopy structure and spatial distribution. Yan et al. applied the SRT model to heterogeneous discrete canopies
55 (Yan et al., 2021), achieving an optimal balance between accuracy and efficiency in modeling radiation regimes of discontinuous canopies. Li et al. (2020) expanded SRT to simulate BRF in forests with within-crown heterogeneity, parameterizing vertical and horizontal foliage distributions to enable simulations of complex canopy structures while maintaining theoretical consistency with 3D radiative transfer (Li et al., 2020). While SRT models have proven effective in characterizing RT within heterogeneous canopies, their performance in mountainous regions is limited by the neglect of terrain
60 effects. Extending the SRT theory to sloping terrain could enhance the characterization of RT within mountain vegetation, providing a more comprehensive understanding of canopy heterogeneity in such challenging environments.



In terms of quantitative impacts on CR modelling, soil reflectance is a key factor in the accurate modeling of canopy reflectance, especially in areas with sparse vegetation. Under canopies with a low leaf area index (LAI < 2), soil reflectance can contribute significantly to the total canopy reflectance, particularly in the near-infrared (NIR) region (Jacquemoud et al., 65 2009). Neglecting soil reflectance in canopy reflectance (CR) models can lead to errors of 10–30% in reflectance estimates (Baret et al., 1993). Research has shown that incorporating precise soil reflectance data into radiative transfer (RT) models can improve simulation accuracy by 5–15% (Jacquemoud et al., 2009). To better capture the heterogeneity of soil properties across 70 landscapes, empirical methods are commonly used to model soil spectral reflectance. Jiang and Fang (2019) developed the General Spectral Vector (GSV) model, which combines site-specific observational data with soil databases to accurately simulate soil reflectance spectra (Jiang and Fang, 2019). The GSV model has been found to outperform traditional wet chemical methods in soil monitoring (Nocita et al., 2015) and has demonstrated effectiveness in predicting soil properties even in vegetated areas (Pinheiro et al., 2017). -

To address the terrains effects and consider both the heterogeneity of canopy structure and soil properties, a new soil-canopy reflectance model known as GSV-SRTS was developed in this study specifically for sloping heterogeneous landscapes 75 by expanding on the GSV and SRT theory. The canopy gap probability modulated by terrain factors, geotropic growth of vegetation, and terrain-induced variations in illumination and viewing geometry were taken into account. GSV-SRTS can offer a realistic representation of radiation propagation within soil-canopy objects over sloping terrains, serving as a theoretical tool for forward canopy reflectance modeling over sloping terrains with heterogeneous vegetation structures. This model has the potential to be used to accurately retrieve biophysical parameters related to vegetation. To further explore how terrain and 80 vegetation characteristics impact canopy and soil reflectance, the GSV-SRTS model was used to analyse the effects of different terrain factors and canopy gap probabilities on model performance.

The following sections will provide a detailed overview of the article. In Section 2, we will delve into the development of the GSV-SRTS model. Section 3 will outline the evaluation strategy, including the DART configuration and validation using actual remote sensing images. Moving on to Section 4, we will present the results of the validation and performance 85 assessment of the model. Sections 5 and 6 will then offer a discussion of the findings and conclude with final remarks.

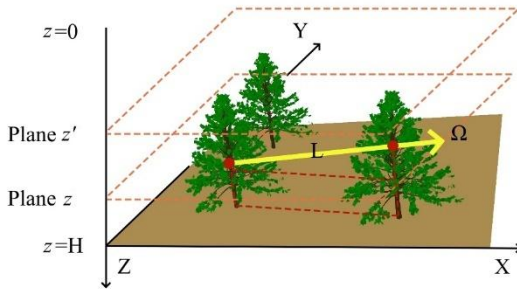
2 Methods

2.1 General Framework of the GSV-SRTS Model

The GSV-SRTS model is a sophisticated theoretical framework designed to address the intricate nature of radiation transfer processes within the layers of a canopy. By expanding upon the traditional radiation transfer equation to include the soil GSV 90 and integrating topographic elements, this model offers a more precise depiction of the inherent variations present in canopy-soil systems. One key feature of the GSV-SRTS model is its utilization of a local slope coordinate system for all internal calculations, ensuring a geometrically accurate representation of how light interacts within a rugged mountainous terrain. To illustrate the application of the GSV-SRTS model, this study presents a 3D discontinuous canopy made up of identical trees



situated within the layer defined as $0 < z < H$ in the coordinate system (Fig. 1) The number of trees housed within a pixel is 95 determined randomly using the Poisson distribution (Huang et al., 2008). From a stochastic view, the 3D canopy structure is conceptualized as a spatial stochastic process, symbolized by an indicator function denoted as $\chi(x, y, z)$. This function yields a value of 1 if the specific point (x, y, z) falls under vegetation cover, and 0 if it does not.



100 **Figure 1: A typical discontinuous vegetation canopy and the coordinate system used for the stochastic RT equation. The planes $z = 0$ and $z = H$ represent the top and bottom boundaries of the vegetation canopy, respectively. A specific point within the vegetation canopy, located on the plane z , moves upward along the unit vector Ω , covering a distance L until it reaches the plane z' .**

2.2 Stochastic radiative transfer equation in sloping terrains

For any given global direction Ω , its corresponding local sun zenith angle $\cos\theta_s$ and local view zenith angle $\cos\theta_v$ are calculated as (Gu and Gillespie, 1998):

$$\cos\theta_{s(v)} = \cos\theta_g \cos\theta'_{s(v)} + \sin\theta_g \sin\theta'_{s(v)} \cos\varphi_{sg(vg)} \quad (1)$$

where θ_g and φ_g represent the slope and aspect, respectively. φ_{sg} is the relative azimuth angle between the sun and the sloping background; and φ_{vg} is the relative azimuth angle between the viewer and the sloping background. All subsequent RT computations inside the canopy are performed using these local angles, ensuring that all physical interactions are relative to the actual inclined surface.

110 The Stochastic Radiative Transfer Equations (SRTE) are obtained through horizontal averaging of the 3D RT process, thereby integrating the influence of canopy structure. Solving these equations (Eqs. (2)-(3)) necessitates determining the mean radiation intensities for both the entire scene, $I(z, \Omega)$, and the vegetation-covered area within a pixel, $U(z, \Omega)$, at depth z in direction Ω , which are defined as (Vainikko, 1973; Shabanov et al., 2000):

$$\mu \frac{\partial \bar{I}(z, \Omega)}{\partial z} = -\sigma'(\Omega) \bar{I}(z, \Omega) + \frac{\sigma_s}{4\pi} \int_{4\pi} \bar{I}(z, \Omega') \sigma'_s(\Omega', \Omega) d\Omega' + F_0(z, \Omega) + F_H(z, \Omega) \quad (2)$$

$$\mu \frac{\partial U(z, \Omega)}{\partial z} = -\sigma'(\Omega) U(z, \Omega) + \frac{\sigma_s}{4\pi} \int_{4\pi} U(z, \Omega') \sigma'_s(\Omega', \Omega) d\Omega' + Q_0(z, \Omega) + Q_H(z, \Omega) \quad (3)$$

115 where $\mu = \cos\theta_v$, and θ is the local view zenith angle. Ω indicates the direction of incoming direct light, and Ω' indicates the viewing direction. $F_0(z, \Omega)$ and $F_H(z, \Omega)$ in Eq.(2) represent the diffuse and direct radiation entering through the upper and lower boundaries. $Q_0(z, \Omega)$ and $Q_H(z, \Omega)$ in Eq. (3) refer to the mean diffuse and direct radiation that penetrate the upper and lower canopy boundaries and subsequently experience scattering in the heterogeneous medium. $\sigma'(\Omega)$ is the extinction coefficient. The extinction coefficient is geometrically corrected to account for local slope-induced projection effects. This correction reduces effective extinction when illumination or viewing directions are highly oblique relative to the local normal, 120



ensuring the local radiative balance remains consistent with the actual slope geometry, which is shown as follows (Mousivand et al., 2015):

$$\sigma'(\Omega) = \sigma(\Omega) \sqrt{\max(0, \mu'_s) \max(0, \mu'_v)} \quad (4)$$

125 The terrain-induced azimuthal dependence of scattering is characterized by a topographic modulation function (S. Sandmeier, 1997):

$$C_{\text{topo}}(\phi_v) = \sin \theta_g \cos \phi_{vg} \mu'_s \mu'_v \quad (5)$$

which enhances scattering in the downslope direction and weakens it in the upslope direction. The scattering kernel $\sigma'_s(\Omega', \Omega)$ in Eq.(2)(3) is adjusted by the slope-induced azimuthal modulation function:

$$\sigma'_s(\Omega', \Omega) = \sigma_s(\Omega', \Omega) [1 + C_{\text{topo}}(\phi_v)] \quad (6)$$

where $\sigma_s(\Omega', \Omega)$ is the original differential scattering coefficient (using a Henyey–Greenstein phase function).

The average horizontal intensity across over vegetated area $U(z, \Omega)$ or the entire horizontal plane $\bar{I}(z, \Omega)$ comprise two components: the direct and the diffuse parts of the incoming irradiance, which can be given as follows (Shabanov et al., 2000):

$$\begin{aligned} U(z, \Omega) &= U_{\text{dir}} \delta(\Omega' - \Omega) + U_{\text{dif}}(z, \Omega) \\ \bar{I}(z, \Omega) &= f_{\text{dir}} I_{\text{dir}} \delta(\Omega' - \Omega) + I_{\text{dif}}(z, \Omega) \end{aligned} \quad (7)$$

135 where f_{dir} is the fraction of incident direct radiation on the upper boundary; $\delta(\Omega' - \Omega)$ is Dirac's delta function (Dirac, 1981), which approaches infinity when the polar angle in direction Ω matches the direction of direct solar radiation Ω , and zero otherwise; $U_{\text{dir}}(z)$ ($I_{\text{dir}}(z)$) and $U_{\text{dif}}(z, \Omega)$ ($I_{\text{dif}}(z, \Omega)$) represent the direct component and the diffuse component over the vegetation-occupied area (or the entire scene area), respectively, which is described in Eq.(7). The boundary conditions for the entire scene are simplified as follows (Shabanov et al., 2000; Bird and Hulstrom, 1981).

$$I_0(z, \Omega) = F_{\text{dir}}(\Omega_0) \delta(\Omega - \Omega_0) + d_0(z, \Omega), u < 0 \quad (8)$$

$$I_H(z, \Omega) = \frac{R(\Omega, \Omega')}{\pi \int_{2\pi^+} R(\Omega, \Omega') \cos \theta_v d\Omega} + d_H(z, \Omega), u > 0 \quad (9)$$

$$\begin{aligned} F_{\text{dir}} &= S_0 \cos \theta_s T \\ \rho_{\text{soil}} &= \frac{1}{\pi} \int_{2\pi^+} R(\Omega, \Omega') \cos \theta_v d\Omega \end{aligned} \quad (10)$$

where $\delta(\Omega - \Omega_0)$ is the Dirac's delta function, which enables precise estimation of the solar radiation. $F_{\text{dir}}(\Omega_0)$ represents the intensity of direct radiation incident on the upper boundary. S_0 is the solar constant, and T is the atmospheric transmittance.

145 $d_0(z, \Omega)$ denotes the diffuse radiation intensity from the upper boundary, while $d_H(z, \Omega)$ represents the intensity entering the canopy through the lower boundary. These two parameters can be calculated using the Second Simulation of the Satellite Signal in the Solar Spectrum (6S) model (Roujean et al., 1992). The 6S model calculates $d_0(z, \Omega)$ as atmospheric diffuse skylight via RTE accounting for Rayleigh and aerosol scattering and $d_H(z, \Omega)$ by integrating surface/canopy scattering effects on transmitted radiation. $R(\Omega, \Omega')$ is the bidirectional soil reflectance factor, the same as $R_{1 \times l}$ in Eq (20) and ρ_{soil} is the soil



150 hemispherical reflectance. The incoming radiation can be parameterized by two values: the total flux $F_{dir+dif}(\Omega_0)$, defined as follows (Shabanov et al., 2000):

$$F_{dir+dif}(\Omega_0) = \int_{2\pi^-} \bar{I}_0(z, \Omega) \cos \theta_v d\Omega = F_{dir} \cos \theta_v + \int_{2\pi^-} d_0 \cos \theta_v d\Omega \quad (11)$$

The horizontal average intensity $U(z, \Omega)$ over the vegetation-covered area can be decomposed into the direct ($U_{dir}(z)$) and diffuse ($U_{dif}(z)$) components of the incoming solar radiation, defined as follows (Shabanov et al., 2000):

$$155 \quad \begin{cases} U_{dir}(z) + \frac{\sigma(\Omega)}{|\cos \theta_v|} \int_0^z K(z, z', \Omega) U_{dir}(z', \Omega) dz' = 1 \\ \left\{ \begin{array}{l} U_{dif}(z, \Omega) + \frac{\sigma(\Omega)}{|\cos \theta_v|} \int_0^z K(z, z', \Omega) U_{dif}(z', \Omega) dz' = \frac{1}{|\cos \theta_v|} \int_0^z K(z, z', \Omega) S_{dif}(z', \Omega) dz' + F_0(z, \Omega), \mu < 0 \\ U_{dif}(z, \Omega) + \frac{\sigma(\Omega)}{|\cos \theta_v|} \int_z^H K(z, z', \Omega) U_{dif}(z', \Omega) dz' = \frac{1}{|\cos \theta_v|} \int_z^H K(z, z', \Omega) S_{dif}(z', \Omega) dz' + F_H(z, \Omega), \mu > 0 \end{array} \right. \end{cases} \quad (12)$$

$$S_{dif}(z', \Omega) = \int_{4\pi} \sigma_s(\Omega \rightarrow \Omega') U_{dif}(z', \Omega') d\Omega' \quad (13)$$

where $S_{dif}(z', \Omega)$ denotes the spherical integration of scattering. $K(z, z', \Omega)$ is the Conditional Probability Correlation Function (PCF). This core function quantifies the probability of spatial correlation between vegetation elements at depths z and z' along direction Ω , thereby statistically capturing the effect of canopy 3D structure and heterogeneity on the radiation field. Its 160 mathematical form is shown as follows (Shabanov et al., 2007):

$$q(z, z', \Omega) = \langle \frac{1}{S} \iint_S \chi(x, y, z) \chi(x', y', z') \cdot f(\theta_g, \Delta h) dx dy \rangle \quad (14)$$

$$f(\theta_g, \Delta h) = \exp\left(-\frac{\Delta h}{H \cdot \tan \theta_g}\right) \quad (15)$$

$$p(z) = \langle \frac{1}{S} \iint_S \chi(x, y, z) dx dy \rangle \quad (16)$$

$$K(z, z', \Omega) = \frac{q(z, z', \Omega)}{p(z)} = \langle \frac{\iint_S \chi(x, y, z) \chi(x', y', z') dx dy}{\iint_S \chi(x, y, z) dx dy} \rangle \quad (17)$$

165 where $p(z)$ is the canopy density at canopy depth z , $\chi(x, y, z)$ is the indicator function (1 for vegetation, 0 otherwise). The point (x, y, z) moves travels a distance L in the direction Ω to reach (x', y', z') . The bracket $\langle \cdot \rangle$ denotes the ensemble average over all realizations of $\chi(x, y, z)$ within a finite pixel. Δh is the vertical elevation difference between two points, H is the total vertical height of the vegetation canopy.

2.3 Reflectance factors of the soil background

170 Soil reflectance properties are important elements that should be carefully formulated in canopy radiative transport process modelling (Knyazikhin et al., 1998b; Verhoef and Bach, 2007). However, modelling soil reflectance is challenging due to the complex optical properties of soil in shortwave bands. The GSV soil reflectance model addresses this by providing an effective method for approximating the reflectance spectra of both dry and wet soils (Jiang and Fang, 2019). The GSV refers to the soil



175 spectral vector, which can be obtained by integrating dry and wet soil data. The global soil reflectance matrix $R_{m \times l}$ can be
expressed as follows (Jiang and Fang, 2019):

$$R_{m \times l} \approx U_{m \times m} \Sigma_{m \times l} V_{l \times l} \quad (18)$$

where m represents the number of dry soil samples; l represents the number of bands; and $R_{m \times l}$ represents the dry soil spectral matrix. $U_{m \times m}$, $\Sigma_{m \times l}$, and $V_{l \times l}$ can be calculated by the Python callable function *svd* (singular value decomposition).

180 Principal component analysis is used to obtain $\Sigma_{m \times n}$ and $V_{n \times l}$, where $V_{n \times l}$ takes the first few vectors. $U_{m \times m} \Sigma_{m \times n}$ can be written as $C_{m \times n}$. For our GSV model, instead of m row vectors, $C_{1 \times (n+1)}$ is needed, which can be expressed as follows (Jiang and Fang, 2019):

$$C_{1 \times (n+1)} = R_{1 \times d} V_{(n+1) \times d}^{-1} \quad (19)$$

185 where $R_{1 \times d}$ represents the soil spectral data from the region of interest. The first several rows of $V_{(n+1) \times d}$ can account for the first n rows of $V_{(n+1) \times d}$ because we take the first several vectors through principal component analysis. The $n+1$ row of $V_{(n+1) \times d}$ represents the vector of the n rows of wet soil and one soil spectral data of the study area. Finally, the reflectance spectrum of the soil background can be calculated as follows (Jiang and Fang, 2019):

$$R_{1 \times l} = C_{1 \times (n+1)} V_{(n+1) \times l} \quad (20)$$

where $R_{1 \times l}$ is the final soil spectral vector.

2.4 BRF Calculation

190 The discrete ordinates method, a standard approach for solving radiative transfer problems, was used to numerically solve the coupled SRTS system with its boundary conditions. The incoming radiation is parameterized by the total flux $F_{dir+dif}(\Omega_0)$ (Shabanov et al., 2000). The horizontal average intensities $\bar{I}(z, \Omega)$ and $U(z, \Omega)$ are divided into direct and diffuse components for computational solution. The final simulated BRF is calculated from the resulting upwelling radiation intensity at the canopy top ($z = 0$) for the viewing direction Ω_v :

$$195 \text{BRF}(\Omega_v, \Omega_s) = \frac{\pi \cdot \bar{I}(0, \Omega_v)}{F_{dir}(\Omega_s) + E_{diff}} \quad (21)$$

where $E_{diff} = \int_{2\pi} d_0(\Omega) |\cos\theta_v| d\Omega$ is the total diffuse irradiance on the horizontal plane.

3 Dataset

3.1 Strategy for Evaluating the Performance of the SRTS Model

200 To comprehensively evaluate the proposed GSV-SRTS model, the simulations were conducted as follows: First, the overall accuracy of GSV-SRTS was evaluated against DART using scatterplots to validate the model feasibility. Next, GSV-SRTS was compared with the typical mountain CR models to validate its advantage in various terrain and canopy conditions after incorporating the SRT theory and soil spectral vector. The angular distribution of GSV-SRTS was analyzed to reveal the response mechanism of terrain and canopy conditions to multi-angle observations. Finally, the remote sensing observations



from different sensors were utilized for model evaluation to evaluate the suitability of the GSV-SRTS model in a real
205 mountainous area under various spatial resolutions.,

3.2 Comparison of DART-based Simulation Models

The DART model is a highly regarded analysis tool utilized for modeling the transmission of radiation signals within soil-leaf-canopy systems (Gastellu-Etchegorry et al., 2012). It has the capability to accurately simulate the canopy reflectance in various types of terrain and canopy structures. During the validation of the model, DART simulations were used as the standard to
210 assess the reliability of the GSV-SRTS model as well as other comparable models. In the virtual scenarios created by DART, specific parameters such as the solar zenith angle of 30° and solar azimuth angle of 0° were set. Additionally, to evaluate the performance of the model in multi-angle observations, the view zenith angle was varied from 0° to 60°, while the view azimuth angle ranged from 0° to 360°, encompassing the entire observation hemisphere. To investigate the accuracy of the model across
215 different sloping surfaces, the slope angle was adjusted from 0° to 50° in increments of 10°, covering gentle, moderate, and steep slopes. The aspect was fixed at 0°, 90°, 180° and 270°, corresponding to surfaces facing north, east south and west respectively. Various values of Leaf Area Index (LAI) ranging from 0.5 to 4, canopy height from 2 m to 30 m, and canopy density from 0.1 to 0.8 were set to represent sparse, moderate, and dense vegetation coverage scenarios. The virtual vegetation
220 scenes were standardized at 100×100 m with diverse canopy structures, terrains, and viewing conditions. The specifics of the input parameters for generating scenes in DART are outlined in Table 1. In comparison to traditional mountain canopy reflectance models, the SLCT and GOST2 models were utilized, which are based on radiative transfer and geometrical optical theories for sloping terrains. All results from the compared models were juxtaposed with the DART simulations in the same virtual scenes as the benchmark for accuracy assessment.

Table 1. Specification of the input parameters of the scenes generated by DART

Model Parameters		Units	Range
Leaf parameters			
S_L	Leaf linear characteristic dimension	[m]	0.05-0.2
Canopy structure parameters			
LAI	Leaf area index	[m ² / m ²]	0.5-4
ALA	Average leaf angle	[°]	30
p	Canopy density	unitless	0.1-0.8
H	Canopy height	[m]	2-30
$\chi(x, y, z)$	Indicator function	unitless	0 or 1
Illumination view geometry			
θ_s	Sun zenith angle	[°]	0
θ_v	View zenith angle	[°]	0-360
ϕ_s	Sun azimuth angle	[°]	30
ϕ_v	View azimuth angle	[°]	0-60
Atmospheric condition			



f_{dir}	Diffuse radiation fraction	unitless	0.2
T	Atmospheric transmittance	unitless	0.7
Topographic factors			
θ_g	Slope	[°]	0-60
φ_g	Aspect	[°]	0-360

3.3 Assessment of the Terrain and Canopy Conditions Effects on Multi-angle CR Simulations

225 To discover the influence of canopy structure, multi-angle CR simulations were conducted. The virtual vegetation scenes were set with stable terrain and view conditions. The sun zenith angle was set to 30° and the sun azimuth angle was set to 0°. The view zenith angle was set ranging from 0° to 60°, and the view azimuth angle was set ranging from 0° to 360° to cover the hemispheric viewing space. And the canopy densities were set to 0.2, 0.5 and 0.8 to demonstrate sparse, medium and dense vegetation coverage. On multi-angle CR simulations, the terrain and canopy condition effects were assessed explicitly.

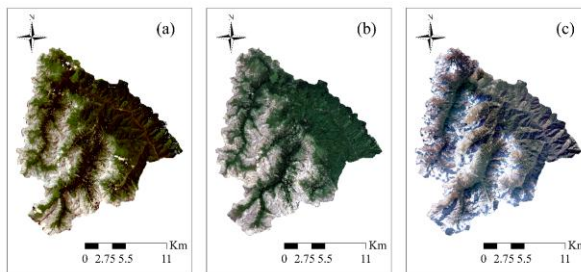
230 **3.4 Assessment of the Terrain and Canopy Conditions Effects on Multi-angle CR Simulations**

To assess the effectiveness of the proposed model, it is imperative to simulate canopy reflectance in a real mountainous setting. The chosen location for this study is the Wanglang Field Observation Station, situated in the northeastern region of the Tibetan Plateau at coordinates approximately 32.94°N and 104.07°E. This area boasts a diverse landscape characterized by towering mountain peaks and deep gorges, with elevations ranging from 2000 to 4200 meters and slopes that can vary from gentle 235 inclines to steep gradients of up to 76°. The various vegetation types that thrive in this unique environment include deciduous forests, coniferous forests, mixed forests combining both coniferous and deciduous species, as well as scrublands.

Satellite products from Landsat 9-OLI, Sentinel-2, and Jilin-1 with spatial resolutions of 30 m, 10 m, and 0.5 m, respectively, are presented in Fig. 2. Cloud-free remote sensing images from these sensors, covering the experimental area, served as reference data for model performance assessment. The Landsat 9-OLI image was acquired on July 30, 2024, during 240 the vegetation growing season, with solar zenith and azimuth angles of 25.5° and 119.6°, respectively. It was obtained from the Earth Resources Observation and Science (EROS) Center Science Processing Architecture (ESPA) on-demand interface (<https://espa.cr.usgs.gov/>), which provides surface reflectance products corrected using the Second Simulation of the Satellite Signal in the Solar Spectrum Vector (6SV) model (Vermote et al., 2016). The Sentinel-2 image was captured on July 8, 2022, with corresponding solar zenith and azimuth angles of 18.73° and 119.2°, and was downloaded from the Copernicus Open 245 Access Hub (<https://dataspace.copernicus.eu/>). The Jilin-1 remote sensing images were acquired and mosaicked from the Jilin-1 Satellite Network (<https://www.j1mall.com/>), with data collected between June and August from 2022 to 2024. These three remote sensing images are accompanied by corresponding digital elevation models (DEMs) for topographic analysis. Topographic factors for the study area were derived from the following sources: the ASTER Global Digital Elevation Model (GDEM) version 2 (spatial resolution of 1 arc-second, approximately 30 m) was used for the Landsat 9-OLI image; the 250 Copernicus DEM GLO-10 product (10 m resolution) was acquired from the Copernicus Open Access Hub to match the



Sentinel-2 image; and high-resolution DEM data were obtained via unmanned aerial vehicle (UAV) laser scanning and resampled to a 0.5 m resolution to align with the Jilin-1 imagery.



255 **Figure 2: Study area Wanglang National Nature Reserve, Pingwu County, Mianyang with three different sources of remote sensing images, from which (a) Landsat9-OLI, (b) Sentinel2, (c) Jilin-1.**

The input parameters for driving the SRTS model are summarized in Table 2. These parameters have been carefully defined using a combination of field measurements, remote sensing products, and relevant literature. For example, the leaf linear characteristic dimension (S_L) has been designated as 0.05-02 m based on typical values for vegetation (Jacquemoud et al., 2009). Canopy structure parameters included in the model consist of a leaf area index (LAI) ranging from 2-4 m^2/m^2 , canopy height (C_H) varying from 5-30 m to encompass the range of measurements, and an average leaf angle (ALA) of 30° which follows an ellipsoidal distribution assumption (Campbell, 1990). In order to accurately capture the topographic variability of the study area, parameters such as slopes (θ_g) ranging from 0-60° and aspects (φ_g) from 0-360° have been incorporated into the model. These parameters ensure that the full terrain characteristics are taken into consideration during the simulations. Furthermore, atmospheric parameters for the study area have been derived using the MODTRAN atmospheric radiative transfer model (Berk et al., 2004). This ensures that the atmospheric conditions are accurately represented in the model simulations. The illumination geometry has been fixed based on remote sensing observations, providing a consistent and reliable input for the model. By incorporating all of these parameters into the SRTS model, we are able to accurately simulate and analyze the surface reflectance properties of the study area.

270 The input parameters for the model are outlined in Table 2, with a summary provided for reference. A dataset based on these parameters was used to generate 10000 combinations of input values. Each combination was then used to compare the remote sensing reflectance with the simulated reflectance stored in a lookup table (LUT) on a pixel-by-pixel basis. In order to mitigate the challenges posed by the ill-posed nature of the model inversions (Vermote et al., 1997) the final outcome was determined by averaging the results from the 100 best-matching simulations. The degree of agreement between the observed 275 and simulated reflectance was evaluated using the following cost function:

$$\text{Cost} = \sqrt{\left(\frac{\text{Sim}_r - \text{Obs}_r}{\text{Obs}_r}\right)^2 + \left(\frac{\text{Sim}_n - \text{Obs}_n}{\text{Obs}_n}\right)^2} \quad (22)$$



where Sim_r and Sim_n are the simulated reflectances in the red and NIR bands, respectively, and Obs_r and Obs_n are the observed reflectances in the red and NIR bands, respectively.

Table 2. Specification of the input parameters to generate the LUT

Model Parameters		Units	Range
Leaf parameters			
S_L	Leaf linear characteristic dimension	[m]	0.05-0.2
Canopy structure parameters			
LAI	Leaf area index	[m^2/m^2]	2-4
ALA	Average leaf angle	[$^\circ$]	30
p	Canopy density	unitless	0.2-0.8
C_H	Canopy height	[m]	5-30
$\chi(x, y, z)$	Indicator function	unitless	0 or 1
Illumination view geometry			
θ_s	Sun zenith angle	[$^\circ$]	25.5
θ_v	View zenith angle	[$^\circ$]	0-360
φ_s	Sun azimuth angle	[$^\circ$]	119.6
φ_v	View azimuth angle	[$^\circ$]	0-60
Atmospheric condition			
f_{dir}	Diffuse radiation fraction	unitless	0.2
T	Atmospheric transmittance	unitless	0.7
Topographic factors			
θ_g	Slope	[$^\circ$]	0-60
φ_g	Aspect	[$^\circ$]	0-360



280 **4 Results and analysis**

4.1 Model Evaluation by DART and Typical CR Models

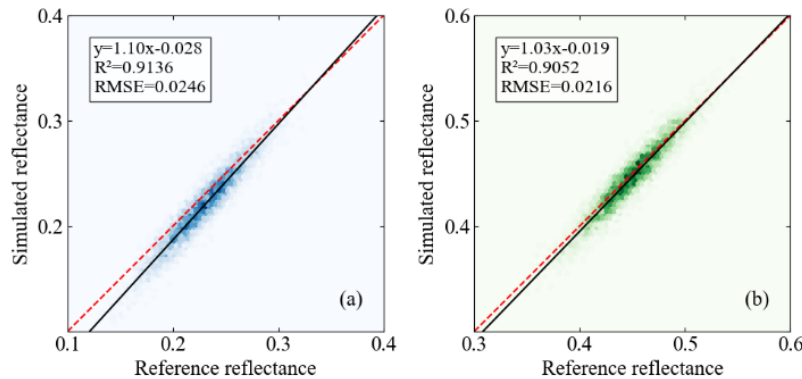


Figure 3: Density scatterplots between the canopy reflectance simulated by DART and the GSV-SRTS models. (a) and (b) represent the DART simulations compared with the SRTS model in the red and NIR bands.

285 To validate the overall simulation accuracy of the GSV-SRTS model, the GSV-SRTS simulations were compared against the DART simulations. As shown in Fig. 3 and Fig. 4, the scatter plots were generated using comprehensive input parameter combinations, including varying slope, aspect, canopy density, and observation direction. The results showed that GSV-SRTS achieved the highest R^2 value of 0.9136 (0.9052) and the lowest RMSE of 0.0146 (0.0106) in the red (NIR) band, outperforming other compared models.

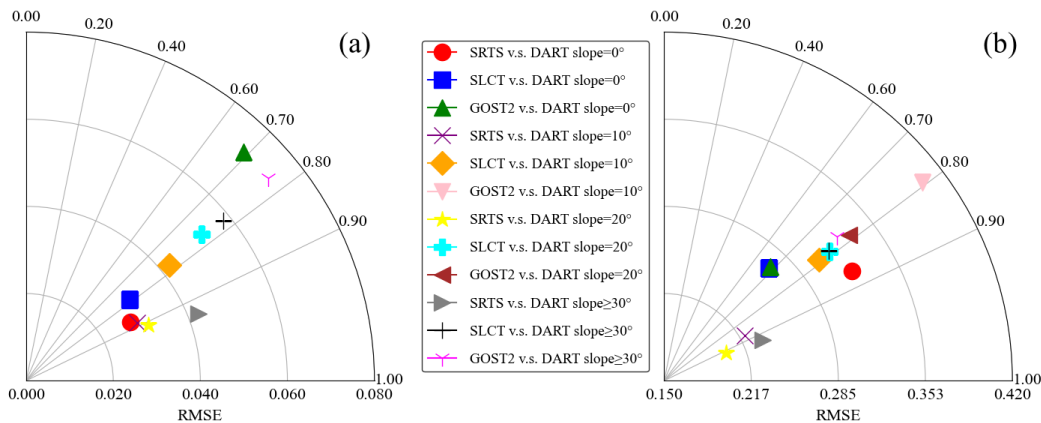


Figure 4: The comparison between GSV-SRTS, SLCT, GOST2, and DART over different sloping terrains. (a) and (b) represent the results in the red and NIR bands, respectively.

290 As shown in Figure 4, the model comparison across different slopes shown that the GSV-SRTS and DART simulations have good consistency over different sloping terrains. In comparisons between DART and other models, the performance of GOST2 and SLCT deteriorates as slope increases. The SLCT model, which assumes trees grow perpendicular to the ground, 295 exhibits distortions in simulating crown gap fraction on steeper slopes. This in turn affects the accurate characterization of



radiation contributions over sloping terrain. GOST2 assumes that trees follow the Neyman type-A distribution pattern (Fan et al., 2015). Although the GOST2 model can accurately describe the spatial distribution of the trees, the scenes generated by DART where trees are randomly distributed is more suitable for SRTS. Specifically, in the red (NIR) band, SRTS precision 300 increases from 0.8702 (0.8635) at 0° to 0.9318 (0.9234) at slopes $\geq 30^\circ$. This comparison demonstrates enhanced capability of SRTS in complex terrain conditions.

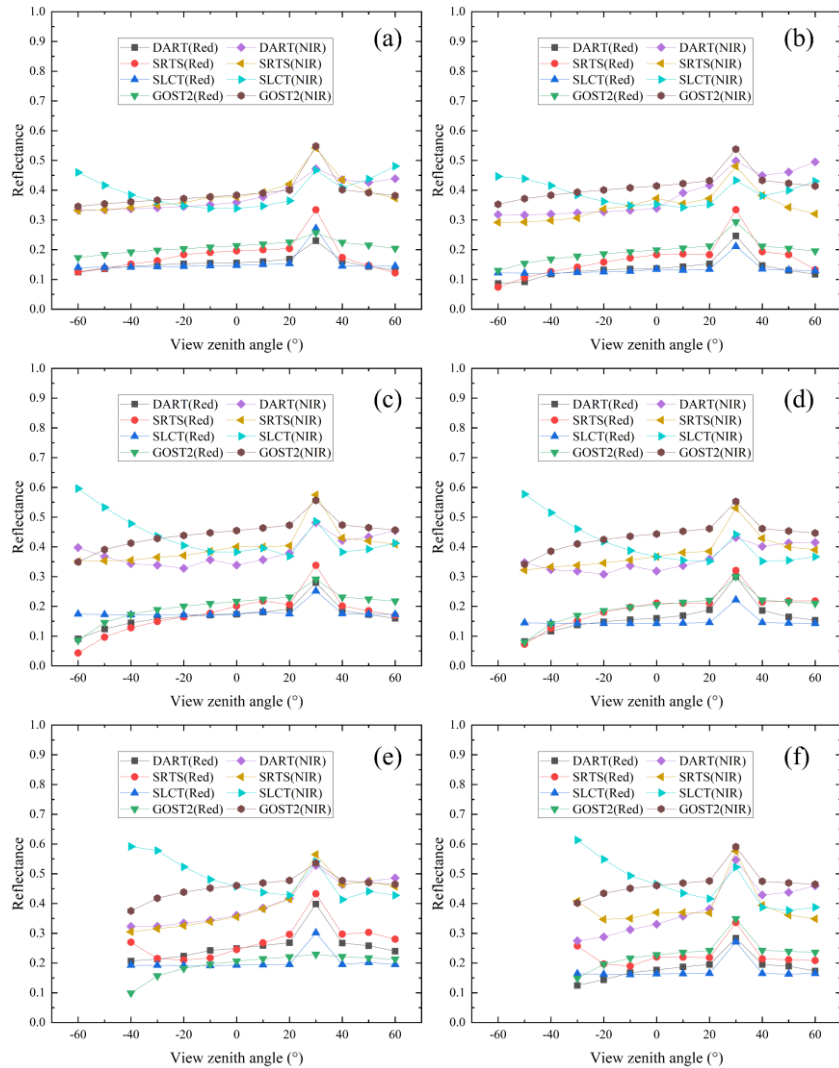


Figure 5: Comparison of canopy reflectance simulated by SRTS, SLCT, and GOST2 models in the PP (principal plane) for slopes of (a) 0°, (b) 10°, (c) 20°, (d) 30°, (e) 40°, and (f) 50°. A view azimuth angle of 0° corresponds to the positive X-axis direction, while 180° corresponds to the negative X-axis direction.

To specifically compare the reflectance under different view zenith angles, the different slopes were set from 0° to 50° with an interval of 10°, as illustrated in Fig. 5. As the terrain slope increases, the GSV-SRTS model achieves the best match with DART simulations in the red and NIR bands, despite SLCT performing better on flat terrain. As the slope steepens, the



fundamental differences in physical approach of each model become increasingly apparent. The SLCT model relies on the
310 simplified plane-parallel RT theory, assuming homogeneous leaf distribution and ignoring slope-induced shadowing effects. This leads to systematic underestimation of multiple scattering contributions in steeper terrain. The GOST2 assumes that the trees follow the Neyman type-A distribution, so when view zenith angle is near nadir, the probability of observing the background is larger than that of the other compared models. The GSV-SRTS model accounts for terrain conditions by coupling a voxel-based canopy representation with a Monte Carlo photon-tracking approach, enabling it to resolve anisotropic
315 scattering patterns caused by tilted surfaces. This ability to adjust and remain accurate even in more complex conditions makes GSV-SRTS especially well-suited for sloping terrains.

4.2 Terrain Effects on CR in Hemispheric Space

To reveal the effects of terrain factors and viewing conditions to canopy reflectance, the angular distributions of reflectance under various scenarios were simulated by the GSV-SRTS model. The results are presented in the form of polar coordinate
320 maps. In these maps, the radial distance corresponds to the zenith angle, while the angular position represents the viewing azimuth angle. The polar contour maps for the red and NIR bands are displayed in Fig. 6 and Fig. 7, respectively.

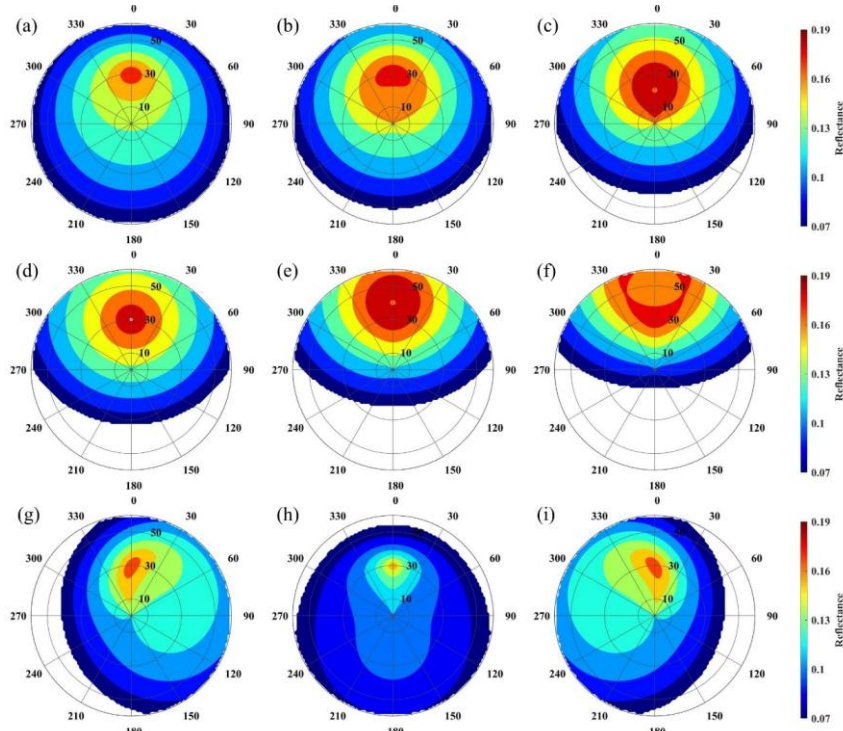


Figure 6: Angular distribution of canopy reflectance in the red band: (a-f) for an aspect of 0° and slopes of $0^\circ, 10^\circ, 20^\circ, 30^\circ, 40^\circ$, and 50° ; (g-i) for a slope of 20° and aspects of $90^\circ, 180^\circ$, and 270° .

325 As shown in Fig. 6, reflectance in the red band ranges primarily between 0.07 and 0.19. The peak of reflectance occurs at the hotspot, where the view zenith angle is 30° and the azimuth angle is 0° . At the same azimuth angle, reflectance decreases



as the zenith angle increases. This angular dependence occurs due to geometric shadowing, path length effects and volume scattering reduction. Photons penetrating the canopy at off-nadir angles traverse longer effective path lengths through the vegetation medium, enhancing absorption by the canopy.

330 When the aspect is 0° (facing the illumination direction), increasing the slope expands the high-reflectance zone and intensifies maximum reflectance at the azimuth angle of 0° . This amplification occurs because steeper slopes facing the light source create optimal conditions for enhanced canopy reflectance. The tilted surface exposes a larger area to direct solar radiation, enhancing the sunlight received by slope-facing vegetation by a factor of $1/\cos\theta$ (where θ is slope angle) (Dubayah and Rich, 1995). On the slope of 20° , solar radiation increases by 64% compared to that in flat terrain.

335 However, when the slope reaches 20° and the aspect shifts to 90° (panel (g)) or 270° (panel (i)), high reflectance concentrates in specific sections of the upper hemisphere. Reflectance is higher between azimuth angles of 0° – 90° in panel (g) and 270° – 360° in panel (i) because the probability of sunlight reaching the ground becomes larger. For slopes with an aspect of 90° , maximum reflectance occurs when the solar azimuth angle is approximately 90° . The PP (principal plane) of incidence is the same with the normal vector of the slope, minimizing the shadowing effects. This geometry enhances the backscatter 340 direction observed by the sensor. It also creates minimal cast shadows and maximum visible illuminated areas, increasing the apparent reflectance. Similarly, slopes with a 270° aspect exhibit peak reflectance near a solar azimuth angle of 270° , following the same geometric principle. Notably, polar contour maps of a 20° slope with aspects of 90° and 270° exhibit symmetry about the vertical axis. This symmetry stems from the fact that the relative azimuth angle between the illumination and viewing directions is the same in both instances. When the sun-sensor geometry is fixed, the reflectance remains consistent, showing 345 mirror-like symmetry around the azimuth of 0° . This confirms that light interacts with slopes in the same way, regardless of their facing direction.

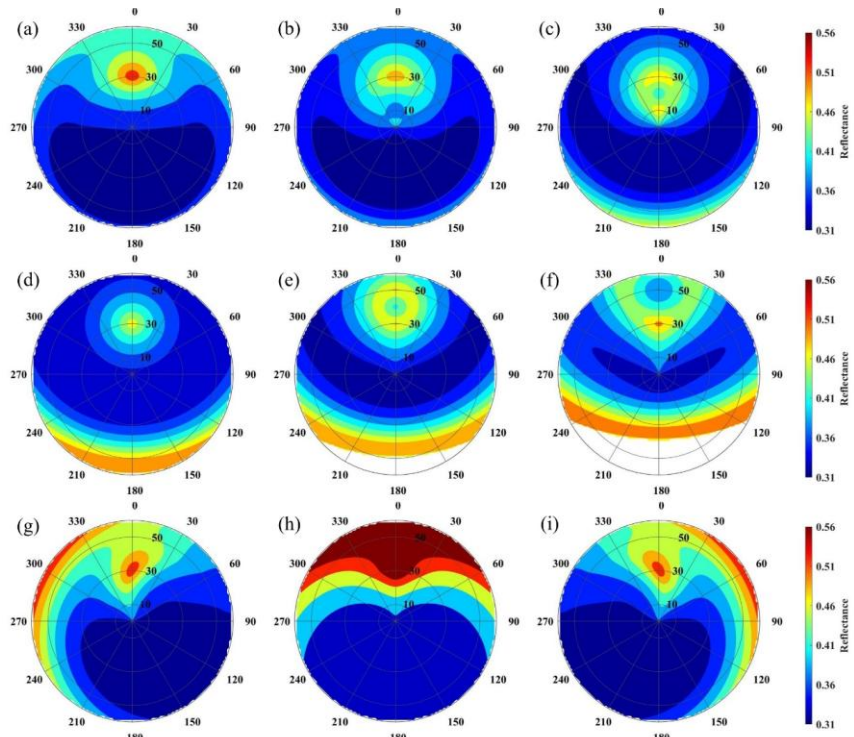


Figure 7: Angular distribution of canopy reflectance in the NIR band: (a-f) for an aspect of 0° and slopes of $0^\circ, 10^\circ, 20^\circ, 30^\circ, 40^\circ$, and 50° ; (g-i) for a slope of 20° and aspects of $90^\circ, 180^\circ$, and 270° .

350

In the NIR band, reflectance displays similar trends yet maintains consistently higher values relative to the red band. As shown in Fig. 7, reflectance ranges primarily from 0.31 to 0.56, with higher values compared to the red band. This difference primarily stems from reduced chlorophyll absorption in the NIR spectrum, enabling more effective light penetration through multiple canopy layers. These distinct interactions lead to characteristically higher NIR reflectance and lower red reflectance in vegetation canopies.

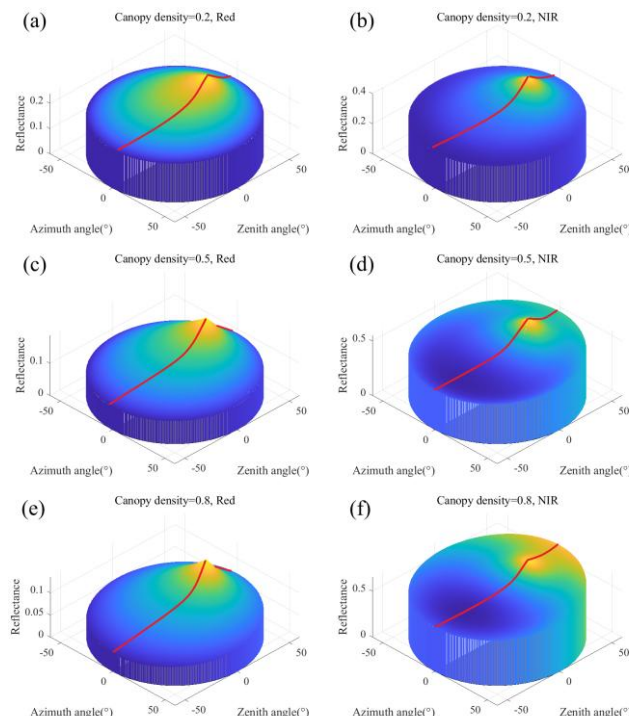
355

When the slope is 20° with the aspect of 90° or 270° , canopy reflectance increases in the hemispherical distribution at the small zenith angles. This demonstrates that steeper slopes facing the sunward direction receive more solar illumination. The consistent slope and illumination direction, combined with symmetrical aspect, result in a symmetrical distribution of gap fractions, which in turn leads to a symmetrical hemispherical reflectance distribution. For a terrain characterized by the slope of 20° facing the aspect of 90° , lower reflectance is concentrated along the 90° - 180° view azimuth angles. In contrast, when the aspect shifts to 270° , reflectance decreases along the 180° - 270° view azimuth directions. When the slope faces 90° , sensors viewing along the azimuths of 90° - 180° observe the sunlit slope but detect reduced reflectance. Because when the solar azimuth equals aspect, the illumination angle on the inclined surface is minimized, reducing casting shadows and increasing the projected sunlit area. This geometry enhances the backscattering direction observed by sensors. The same physical principles apply to the aspect of 270° , where reflectance maxima occur near solar azimuth of 270° , demonstrating symmetrical behaviour across the PP.



These results demonstrated the importance of incorporating topographic factors into GSV-SRTS in mountainous conditions, where terrain-induced factors, solar and view geometries significantly affect canopy reflectance patterns. The ability of GSV-SRTS to account for terrain-related variations ensures more accurate RT process simulations.

4.3 Gap Probabilities Effects on Surface Reflectance in Hemispheric Space



370

Figure 8: Hemispheric views of GSV-SRTS-simulated reflectance over three different canopy densities (a) (b) 0.2, (c) (d) 0.5 and (e) (f) 0.8. The left column represents the canopy reflectance in the red band, and the right column represents the canopy reflectance in the NIR band.

The gap probability, a critical factor influencing the radiative properties of vegetation and soil in remote sensing applications, was utilized in a study to investigate how canopy structure impacts surface reflectance simulations. Using the GSV-SRTS 375 model, the hemispherical distributions of surface reflectance in the red and NIR bands were simulated under different canopy densities. Figure 8 illustrates that canopy reflectance peaks in the hotspot direction, regardless of changes in slope. This directional peak is a result of decreased canopy densities and shadowing from the ground when the sensor's viewing angle aligns with the direction of solar illumination. The GSV-SRTS model accurately captures the reduced probability of observing shaded areas by integrating terrain-modified gap probability and geometries into its simulations. Increasing canopy density 380 leads to a noticeable increase in NIR reflectance (panels (b), (d) (f)) particularly at the nadir, due to enhanced photon interactions within the canopy and changes in gap probability affecting radiation penetration. In contrast, red band reflectance (panels (a), (c) (e)) remains low across all canopy densities, reflecting the strong absorption of red light by chlorophyll.



Therefore, both spectral regions demonstrate significant bidirectional reflectance distribution function (BRDF) effects, with NIR reflectance being more sensitive to changes in canopy density.

385 Moreover, reflectance in the backward-scattering direction consistently exceeds that in the forward-scattering direction. This indicates sunlit crowns become more visible at this direction and mutual shading effects are minimized in this viewing geometry, where the sunlit portions dominate the field of view of sensors. Such directional reflectance features are especially pronounced under dense canopies, where shadowing and multiple scattering further enhance the contrast between forward and backward observations. These reflectance characteristics provide critical understanding of the 3D structure and complexity of
390 forest canopies.

4.4 Model Assessment in a Real Mountainous Region

To assess the effectiveness of the GSV-SRTS model in a practical mountainous setting and explore how well the model works at different levels of detail, we utilized a combination of satellite imagery sources with varying resolutions. Specifically, the Landsat 9-OLI imagery with a resolution of 30 meters, the Sentinel-2 imagery with a resolution of 10 meters, and the Jilin-1
395 imagery with a resolution of 0.5 meters were employed to establish the reference reflectance values for our model evaluation. Additional information regarding the specific geographic area of focus for our study and the technical details of the images can be found in Section 3.4.

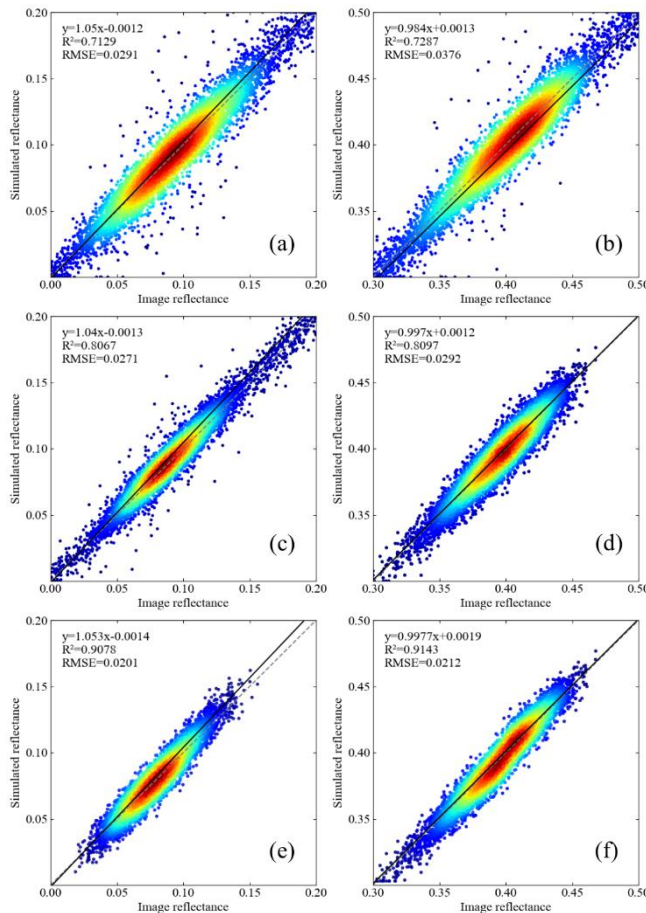


Figure 9: Density scatterplots comparing the simulated reflectance from the SRTS model with the image reflectance for (a) red and (b) NIR bands of Landsat 9-OLI, (c) red and (d) NIR bands of Sentinel-2, and (e) red and (f) NIR bands of JiLin-1.

As illustrated in Fig. 9, the GSV-SRTS-simulated reflectance shows lower R^2 values of 0.7129 (0.7287) and higher RMSE values of 0.0291 (0.0376) in the red (NIR) band when compared with the Landsat9-OLI image reflectance. For the Sentinel-2 image, the SRTS-simulated reflectance achieves R^2 values of 0.8067 (0.8097) and RMSE values of 0.0271 (0.0292) in the red (NIR) band. The SRTS-simulated reflectance shows the highest consistency with the reflectance of the JiLin-1 image, with R^2 values of 0.9078(0.9143) and RMSE values of 0.0201 (0.0212) in the red (NIR) band.

The reflectance simulation accuracy of the GSV-SRTS model enhances with higher spatial resolution of remote sensing images, owing to the ability of the underlying SRT theory and GSV model to resolve finer details in microscale settings. This compatibility stems from the core mechanics of the GSV-SRTS model, which simulates photon interactions within the canopy in detail. The model incorporates key processes, including multiple scattering between leaves, leaf orientation, shadowing effects, and canopy structure variation. And the soil background is fully considered and accurately modelled. Consequently, the GSV-SRTS model is highly compatible with high-resolution imagery. Coarser resolution images tend to smooth out small-



scale features, limiting the ability of the model to leverage its detailed photon-tracking capabilities. In contrast, high-resolution images preserve the finer details, more complex and heterogeneous conditions need to be considered in model development.

As a result, the GSV-SRTS model achieves optimal accuracy with high-resolution images, producing more realistic 415 reflectance estimates. Therefore, the integration of high-resolution data with the photon-sensitive framework of the GSV-SRTS model enables precise capture of subtle canopy reflectance variations, optimizing model performance and achieving highly precise results.

5 Discussion

Accurate modeling of soil-canopy radiation interactions is essential for retrieving biophysical variables at regional-to-global 420 scales. However, topographic relief and heterogeneous landscapes introduce significant uncertainties in radiative transfer simulations. While numerous canopy reflectance models account for sloping terrain, most cannot take heterogeneities of canopy structure and soil properties into account, leading to distorted BRDF patterns (Xiaowen et al., 1993; Gastellu-Etchegorry et al., 1996; Chen and Leblanc, 1997). This study proposed a CR model by extending the GSV and the stochastic 425 RT model for Sloping Terrains (GSV-SRTS), improving the model applicability in real mountainous environments. The GSV-SRTS model advances vegetation and soil reflectance modeling because of its physically based BRDF framework, which intrinsically accounts for 3D canopy structure and surface interactions (Jean-Lucwidlowski et al., 2015).

However, the study still has limitations in the theoretical framework and experimental design, requiring further improvement. Although the GSV-SRTS model incorporates terrain effects, the influence of the surrounding terrains was 430 neglected. In mountainous regions, varying slope angles significantly affect RT by altering shadow patterns, neglecting the adjacent terrain irradiance may increase inaccuracies in remote sensing modeling, especially for the surface coverage with high reflectance (Mousivand et al., 2015; Rich and M., 1995; Sandmeier and Itten, 1997). The surrounding terrains may block direct solar radiation, reducing incident energy on the target surface (Riaño et al., 2003). Surrounding terrain surfaces scatter 435 indirect radiation, altering the total flux received by the canopy (Gu and Gillespie, 1998). Concave landforms (e.g., valleys) enhance multiple reflections, while convex features (e.g., ridges) redistribute local energy budgets (Soenen et al., 2005; Chen and Black, 1992). Future studies should explore integrating surrounding terrain effects into the GSV-SRTS model to enhance accuracy under different terrains (Knyazikhin et al., 1998a).

The General Spectral Vector (GSV) was originally derived from the LUCAS global soil database, which comprises 440 reflectance spectra from 19,036 dry soil samples (Jiang and Fang, 2019). While this dataset provides a robust foundation for modeling soil optical properties, its applicability to larger-scale or diverse regional studies remains limited due to geographical and pedological constraints. To enhance the generalizability and accuracy of the GSV-PROSAILT model across varied ecosystems and soil types, it is essential to expand the GSV framework by incorporating a broader and more diverse set of soil samples. This expansion would strengthen the model's utility for vegetation-soil radiative transfer modeling by enabling a more accurate representation of spatial variability in soil composition, moisture content, and surface conditions. As emphasized



445 by Jiang and Fang (2019), extending the spectral library with additional representative samples is a critical step toward
achieving higher predictive performance and broader operational applicability in remote sensing applications.

450 The integration of the shoot-level clumping index into GSV-SRTS corrects the bias inherent in the random leaf
distribution assumption, thereby achieving a more realistic characterization of leaf spatial heterogeneity (Chen and Leblanc,
1997; Kuusk, 1985). Chen's hierarchical approach (shoot-tree-stand) addressing aggregation effects suggests that the GSV-
SRTS could further refine the scale dependence of radiative transfer, such as distinguishing between intra- and inter-cluster
scattering contributions (Qin and Goel, 1995). Leaf aggregation alters canopy gap distribution, thereby influencing hotspot
characteristics (He et al., 2012). Incorporating clumping index into SRTS may optimize reflectance simulations in hotspot
directions, particularly in densely vegetated areas (Jupp et al., 1989). The quantitative method for leaf aggregation provides a
theoretical foundation for improving radiative transfer parameterization in GSV-SRTS (Manninen et al., 2005).

455 The current model uses a simplified pair-correlation function (PCF) to represent vegetation spatial structures, reducing
computational demands. However, higher-order moments (e.g., three- or four-point correlation functions) in canopy structure
could improve radiative characteristic predictions (Huang et al., 2008; Tang et al., 2014; Lewis and Disney, 2007). Although
integrating higher-order moments would increase computational load, advancements in parallel computing and GPU
technology provide potential solutions (Jonckheere et al., 2004; Lovell et al., 2003).

460 Moreover, field sampling efforts are hampered by the complex terrain and hindered by the dense vegetation cover within
the study area. Increasing observation frequency and optimizing sampling schemes could enhance data representativeness
(Lefsky et al., 2002). However, obtaining the canopy structure parameters in mountainous areas is challenging, which can
refine the RT mechanisms (Nelson, 2009). Integrating advanced sensing techniques like LiDAR provide a feasible solution
for addressing these limitations (Yang et al., 2019; Bailey et al., 2020).

465 6 Conclusion

This study proposes a canopy reflectance model, the GSV-SRTS model, which is based on the extended GSV and stochastic
radiative transfer theory. The model is designed to accurately analyse canopy reflectance in sloping heterogeneous landscapes.
To assess the effectiveness of the GSV-SRTS model, comparisons were made with DART simulations, typical CR models,
and remote sensing observations with multiple spatial resolutions. The results of the study indicate that the GSV-SRTS model
470 adequately captures the variations in canopy reflectance induced by terrain and vegetation conditions. It exhibits strong
consistency with DART benchmarks, with the DART benchmarks ($R^2 = 0.9136$ (0.9052), RMSE = 0.0246 (0.0216) in the red
(NIR) band). And this study revealed the influences of various terrain and vegetation conditions on multi-angle CR simulations.
By comparing the GSV-SRTS model with remote sensing observations, it was found that the model is suitable for soil-canopy
radiative transfer modelling in small-scale scenes, with RMSE (R^2) values of 0.0201 (0.9078) for the red band and 0.0212



475 (0.9143) for the NIR band. Therefore, the development of the GSV-SRTS model provides a feasible paradigm for CR modeling and can be used as a potential tool biophysical parameter retrieval.

Code and data availability. The current version of GSV-SRTS code and dataset is available from figshare website <https://doi.org/10.6084/m9.figshare.30392938> (Li, 2025) (Creation date: 2025-10-19).

480

Author contributions. Conceptualization, Guyue Hu and Shaoda Li; methodology, Jinhu Bian and Guyue Hu.; software, Siqi Li and Chenghao Liu; validation, Ronghao Yang and Junxiang Tan. formal analysis, Siqi Li; investigation, Siqi Li and Chenghao Liu; resources, Guyue Hu and Shaoda Li; data curation, Junxiang Tan and Ronghao Yang.; writing—original draft preparation, Siqi Li; writing—review and editing, Guyue Hu; visualization, Siqi Li; supervision, Jinhu Bian; project 485 administration, Shaoda Li; funding acquisition, Guyue Hu, Ronghao Yang, Shaoda Li and Jinhu Bian.

Competing interests. The authors declare that they have no known competing financial interests or personal relationships that could have appeared to influence the work reported in this paper.

490

Disclaimer. Publisher's note: Copernicus Publications remains neutral with regard to jurisdictional claims made in the text, published maps, institutional affiliations, or any other geographical representation in this paper. While Copernicus Publications makes every effort to include appropriate place names, the final responsibility lies with the authors. Also, please note that this paper has not received English language copy-editing. Views expressed in the text are those of the authors and do not necessarily reflect the views of the publisher.

495

Acknowledgements. This research was funded by the National Natural Science Foundation project of China, grant number 42401425, by the General Program of National Natural Science Foundation of China, grant number 42465006, by the National Key Research and Development Program of China, grant number 2020YFA0608702 and by the Science and Technology Research Program of Institute of Mountain Hazards and Environment, Chinese Academy of Sciences, grant number IM-HE-500 CXTD-03.

References

Bailey, B. N., León, M. A. P. d., and Krayenhoff, E. S.: One-dimensional models of radiation transfer in heterogeneous canopies: A review, re-evaluation, and improved model, Copernicus GmbH, 2020.

Baret, F., Jacquemoud, S., and Hanocq, J.-F.: The soil line concept in remote sensing, *Remote Sensing Reviews*, 7, 65-82, 1993.

Berk, A., Anderson, G. P., Acharya, P. K., Bernstein, L. S., and Lewis, P. E.: MODTRAN5: a reformulated atmospheric band model with auxiliary species and practical multiple scattering options, *Proceedings of SPIE - The International Society for Optical Engineering*, 5425, 341-347, 2004.



510 Bird, R. E. and Hulstrom, R. L.: Simplified clear sky model for direct and diffuse insolation on horizontal surfaces, *Solar Energy Research Inst.(SERI)*, Golden, CO (United States), 1981.

Bruno Combal, H. I., and Craig Trotter: Extending a Turbid Medium BRDF Model to Allow Sloping Terrain with a Vertical Plant Stand, *IEEE TRANSACTIONS ON GEOSCIENCE AND REMOTE SENSING*, 2000.

Campbell, G. S.: Derivation of an angle density function for canopies with ellipsoidal leaf angle distributions, *Agricultural and Forest Meteorology*, 49, 173-176, 1990.

515 Chen, J. M. and Black, T. A.: Defining leaf area index for non-flat leaves, *Agricultural & Forest Meteorology*, 15, 421-429, 1992.

Chen, J. M. and Leblanc, S. G.: A four-scale bidirectional reflectance model based on canopy architecture, *IEEE Transactions on geoscience and remote sensing*, 35, 1316-1337, 1997.

Dirac, P. A. M.: *The principles of quantum mechanics*, 27, Oxford university press1981.

520 Dubayah, R. and Rich, P. M.: Topographic solar radiation models for GIS, *International journal of geographical information systems*, 9, 405-419, 1995.

Fan, W., Li, J., and Liu, Q.: GOST2: The Improvement of the Canopy Reflectance Model GOST in Separating the Sunlit and Shaded Leaves, *IEEE Journal of Selected Topics in Applied Earth Observations and Remote Sensing*, 8, 1423-1431, 10.1109/jstars.2015.2413994, 2015.

525 Fan, W., Chen, J. M., Weimin, J., and Gaolong, Z.: GOST: A Geometric-Optical Model for Sloping Terrains, *IEEE Transactions on Geoscience and Remote Sensing*, 52, 5469-5482, 10.1109/tgrs.2013.2289852, 2014.

Gastellu-Etchegorry, J.-P., Grau, E., and Lauret, N.: DART: A 3D model for remote sensing images and radiative budget of earth surfaces, *Modeling and simulation in engineering*, 2012.

530 Gastellu-Etchegorry, J.-P., Demarez, V., Pinel, V., and Zagolski, F.: Modeling radiative transfer in heterogeneous 3-D vegetation canopies, *Remote sensing of environment*, 58, 131-156, 1996.

Gu, D. and Gillespie, A.: Topographic Normalization of Landsat TM Images of Forest Based on Subpixel Sun–Canopy–Sensor Geometry, *Remote Sensing of Environment*, 64, 166-175, 1998.

He, L., Chen, J. M., Pisek, J., Schaaf, C. B., and Strahler, A. H.: Global clumping index map derived from the MODIS BRDF product, *Remote Sensing of Environment*, 119, 118-130, 2012.

535 Hu, G. and Li, A.: BOST: A Canopy Reflectance Model Suitable for Both Continuous and Discontinuous Canopies Over Sloping Terrains, *IEEE Transactions on Geoscience and Remote Sensing*, 60, 1-19, 10.1109/tgrs.2022.3226460, 2022.

Huang, D., Knyazikhin, Y., Wang, W., Deering, D. W., Stenberg, P., Shabanov, N., Tan, B., and Myneni, R. B.: Stochastic transport theory for investigating the three-dimensional canopy structure from space measurements, *Remote Sensing of Environment*, 112, 35-50, 2008.

540 Jacquemoud, S., Verhoef, W., Baret, F., Bacour, C., Zarco-Tejada, P. J., Asner, G. P., François, C., and Ustin, S. L.: PROSPECT+ SAIL models: A review of use for vegetation characterization, *Remote sensing of environment*, 113, S56-S66, 2009.

Jean-Luc Widlowski, Mio, C., Disney, M., Andredakis, J. A. I., and Zenone, F. Z. T.: The fourth phase of the radiative transfer model intercomparison (RAMI) exercise: Actual canopy scenarios and conformity testing, *Remote Sensing of Environment*, 545 169, 418-437, 2015.

Jiang, C. and Fang, H.: GSV: a general model for hyperspectral soil reflectance simulation, *International Journal of Applied Earth Observation and Geoinformation*, 83, 10.1016/j.jag.2019.101932, 2019.

Jonckheere, I., Fleck, S., Nackaerts, K., Muys, B., Coppin, P., Weiss, M., and Baret, F.: Review of methods for in situ leaf area index determination: Part I. Theories, sensors and hemispherical photography, *Agricultural & Forest Meteorology*, 121, 550 19-35, 2004.

Jupp, D., L. B., Strahler, A., H., Woodcock, and C., E.: Autocorrelation and regularization in digital images. II. Simple image models, *Geoscience & Remote Sensing IEEE Transactions on*, 1989.

Knyazikhin, Martonchik, JV, Myneni, RB, Diner, DJ, Running, and SW: Synergistic algorithm for estimating vegetation canopy leaf area index and fraction of absorbed photosynthetically active radiation from MODIS and MISR data, *J GEOPHYS RES-ATMOS*, 1998, 103(D24), 32257-32275, 1998a.

Knyazikhin, Y., Martonchik, J. V., Diner, D. J., Myneni, R. B., Verstraete, M., Pinty, B., and Gobron, N.: Estimation of vegetation canopy leaf area index and fraction of absorbed photosynthetically active radiation from atmosphere-corrected MISR data, *Journal of Geophysical Research-Atmospheres*, 103, 32239-32256, 10.1029/98jd02461, 1998b.



560 Kuusk, A.: The hot-spot effect of a uniform vegetative cover, *Soviet Journal of Remote Sensing*, 3, 645-658, 1985.
Lefsky, M. A., Cohen, W. B., Parker, G. G., Harding, and J., D.: Lidar Remote Sensing for Ecosystem Studies, *Bioscience*, 52, 19-30, 2002.

Lewis, P. and Disney, M.: Spectral invariants and scattering across multiple scales from within-leaf to canopy, *Remote Sensing of Environment*, 109, 196-206, 2007.

565 Li, S.: GSV-SRTS model, doi:10.6084/m9.figshare.30392938, 2025.

Li, X., Huang, H., Shabanov, N. V., Chen, L., Yan, K., and Shi, J.: Extending the stochastic radiative transfer theory to simulate BRF over forests with heterogeneous distribution of damaged foliage inside of tree crowns, *Remote Sensing of Environment*, 250, 112040, 2020.

Lovell, L., B., Jupp, and Culvenor: Using airborne and ground-based ranging lidar to measure canopy structure in Australian forests, *Canadian Journal of Remote Sensing*, 2003.

570 Manninen, T., Stenberg, P., Rautiainen, M., Voipio, P., and Smolander, H.: Leaf area index estimation of boreal forest using ENVISAT ASAR, *IEEE Transactions on Geoscience & Remote Sensing*, 43, 2627-2635, 2005.

Mousivand, A., Verhoef, W., Menenti, M., and Gorte, B.: Modeling top of atmosphere radiance over heterogeneous non-Lambertian rugged terrain, *Remote sensing*, 7, 8019-8044, 2015.

575 Nelson, P. R.: Lidar remote sensing of forest biomass: A scale-invariant estimation approach using airborne lasers, *Remote Sensing of Environment*, 2009.

Nocita, M., Stevens, A., van Wesemael, B., Aitkenhead, M., Bachmann, M., Barthès, B., Dor, E. B., Brown, D. J., Clairotte, M., and Csorba, A.: Soil spectroscopy: an alternative to wet chemistry for soil monitoring, *Advances in agronomy*, 132, 139-159, 2015.

580 Pinheiro, É. F., Ceddia, M. B., Clingensmith, C. M., Grunwald, S., and Vasques, G. M.: Prediction of soil physical and chemical properties by visible and near-infrared diffuse reflectance spectroscopy in the central Amazon, *Remote Sensing*, 9, 293, 2017.

Qin, W. and Goel, N. S.: An evaluation of hotspot models for vegetation canopies, *Remote Sensing Reviews*, 13, 121-159, 1995.

585 Riaño, D., Chuvieco, E., Salas, J., and Aguado, I.: Assessment of different topographic corrections in Landsat-TM data for mapping vegetation types (2003), *IEEE Transactions on Geoscience & Remote Sensing*, 41, 1056-1061, 2003.

Rich, R. D. and M., P.: Topographic solar radiation models for GIS, *International journal of geographical information systems*, 1995.

Ross, J.: The radiation regime and architecture of plant stands, Springer Science & Business Media2012.

590 Roujean, J. L., Leroy, M., and Deschamps, P. Y.: A bidirectional reflectance model of the Earth's surface for the correction of remote sensing data, *Journal of Geophysical Research: Atmospheres*, 97, 20455-20468, 1992.

S. Sandmeier, K. I. I.: A physically-based model to correct atmospheric and illumination effects in optical satellite data of rugged terrain, *IEEE Transactions on Geoscience and Remote Sensing*, 35, 708-717, 1997.

Sandmeier, S. and Itten, K. I.: A physically-based model to correct atmospheric and illumination effects in optical satellite data of rugged terrain, *Geoscience & Remote Sensing IEEE Transactions on*, 35, 708-717, 1997.

595 Schaaf, C. B., Li, X., and al., e.: Topographic effects on bidirectional and hemispherical reflectances calculated with a geometric-optical canopy model, *IEEE Transactions on Geoscience and Remote Sensing*, 32, 1186-1193, 1994.

Shabanov, N. V., Knyazikhin, Y., Baret, F., and Myneni, R. B.: Stochastic modeling of radiation regime in discontinuous vegetation canopies, *Remote Sensing of Environment*, 74, 125-144, 2000.

Shabanov, N. V., Huang, D., Knjazikhin, Y., Dickinson, R., and Myneni, R. B.: Stochastic radiative transfer model for mixture of discontinuous vegetation canopies, *Journal of Quantitative Spectroscopy and Radiative Transfer*, 107, 236-262, 2007.

600 Soenen, S. A., Peddle, D. R., and Coburn, C. A.: SCS+C: a modified Sun-canopy-sensor topographic correction in forested terrain, *IEEE Transactions on Geoscience and Remote Sensing*, 43, 2148-2159, 10.1109/tgrs.2005.852480, 2005.

Tang, H., Dubayah, R., Brolly, M., Ganguly, S., and Zhang, G.: Large-scale retrieval of leaf area index and vertical foliage profile from the spaceborne waveform lidar (GLAS/ICESat), *Remote Sensing of Environment*, 154, 8-18, 2014.

605 Vainikko, G.: Transfer approach to the mean intensity of radiation in non-continuous clouds, *Trudy MGK SSSR, Meteorological Investigations*, 21, 28-37, 1973.



Verhoef, W. and Bach, H.: Coupled soil–leaf–canopy and atmosphere radiative transfer modeling to simulate hyperspectral multi-angular surface reflectance and TOA radiance data, *Remote Sensing of Environment*, 109, 166–182, 10.1016/j.rse.2006.12.013, 2007.

610 Verhoef, W. and Bach, H.: Simulation of Sentinel-3 images by four-stream surface–atmosphere radiative transfer modeling in the optical and thermal domains, *Remote Sensing of Environment*, 120, 197–207, 10.1016/j.rse.2011.10.034, 2012.

Vermote, E., Justice, C., Claverie, M., and Franch, B.: Preliminary analysis of the performance of the Landsat 8/OLI land surface reflectance product, *Remote sensing of environment*, 185, 46–56, 2016.

615 Vermote, E. F., Tanré, D., Deuze, J. L., Herman, M., and Morcette, J.-J.: Second simulation of the satellite signal in the solar spectrum, 6S: An overview, *IEEE transactions on geoscience and remote sensing*, 35, 675–686, 1997.

Verrelst, J., Camps-Valls, G., Muñoz-Marí, J., Rivera, J. P., Veroustraete, F., Clevers, J. G., and Moreno, J.: Optical remote sensing and the retrieval of terrestrial vegetation bio-geophysical properties—A review, *ISPRS Journal of Photogrammetry and Remote Sensing*, 108, 273–290, 2015.

620 Wen, J., Liu, Q., Xiao, Q., Liu, Q., You, D., Hao, D., Wu, S., and Lin, X.: Characterizing Land Surface Anisotropic Reflectance over Rugged Terrain: A Review of Concepts and Recent Developments, *Remote Sensing*, 10, 10.3390/rs10030370, 2018.

Widlowski, J. L., Pinty, B., Lopatka, M., Atzberger, C., Buzica, D., Chelle, M., Disney, M., Gastellu-Etchegorry, J. P., Gerboles, M., and Gobron, N.: The fourth radiation transfer model intercomparison (RAMI-IV): Proficiency testing of canopy reflectance models with ISO-13528, *Journal of Geophysical Research: Atmospheres*, 118, 6869–6890, 2013.

625 Xiaowen, L., Jindi, W., Yi, L., Xiaoyan, Z., and Strahler, A. H.: A Hybrid Geometric Optical and Radiative Transfer Approach for Modeling BRDF of Discontinuous Canopies, 1993.

Yan, K., Zhang, Y., Tong, Y., Zeng, Y., Pu, J., Gao, S., Li, L., Mu, X., Yan, G., Rautiainen, M., Knyazikhin, Y., and Myneni, R. B.: Modeling the radiation regime of a discontinuous canopy based on the stochastic radiative transport theory: Modification, evaluation and validation, *Remote Sensing of Environment*, 267, 10.1016/j.rse.2021.112728, 2021.

630 Yang, B., Knyazikhin, Y., Xie, D., Zhao, H., Zhang, J., and Wu, Y.: remote sensing influence of leaf specular reflection on canopy radiative regime using an improved version of the stochastic radiative transfer model, 2019.

Yin, G., Li, A., Zhao, W., Jin, H., Bian, J., and Wu, S.: Modeling Canopy Reflectance Over Sloping Terrain Based on Path Length Correction, *IEEE Transactions on Geoscience and Remote Sensing*, 55, 4597–4609, 10.1109/tgrs.2017.2694483, 2017.

635 Zeng, Y., Li, J., Liu, Q., Huete, A. R., Xu, B., Yin, G., Fan, W., Ouyang, Y., Yan, K., Hao, D., and Chen, M.: A Radiative Transfer Model for Patchy Landscapes Based on Stochastic Radiative Transfer Theory, *IEEE Transactions on Geoscience and Remote Sensing*, 58, 2571–2589, 10.1109/tgrs.2019.2952377, 2020.